Full Length Article

Spatially ensemble of polydopamine-protected-Au nanocrystals on Fe₃O₄@SiO₂@γ-AlOOH microflower for improving catalytic performance

Linfeng Bai [a,1], Kezhu Xu [c,1], Wanquan Jiang [a,*], Min Sang [a], Qunling Fang [c,*], Shouhu Xuan [b], Xinglong Gong [b,*]

[a] Department of Chemistry, University of Science and Technology of China (USTC), Hefei, Anhui 230026, PR China
[b] CAS Key Laboratory of Mechanical Behavior and Design of Materials, Department of Modern Mechanics, University of Science and Technology of China, Hefei, Anhui 230027, PR China
[c] School of Food and Biological Engineering, Key Laboratory of Metabolism and Regulation for Major Diseases of Anhui Higher Education Institutes, Hefei University of Technology, Hefei, 230009, PR China

ARTICLE INFO

ABSTRACT

Advanced nanocatalysts integrating with high activity and recyclability is one of the most important issues in heterogeneous catalysis. Magnetic hierarchical nanostructures comprising noble metal nanocrystals confined within a protecting penetrable shell will be favored as an efficient candidate toward robust catalytic reactions. This work reports a proof-of-concept magnetic separable nanocatalyst with the polydopamine (PDA)-confined-Au-nanocrystals assembled on the hierarchical surface of Fe₃O₄@SiO₂@γ-AlOOH microflower (Fe₃O₄@SiO₂@γ-AlOOH@Au/PDA). Because of the high surface area of γ-AlOOH hierarchical nanoarchitectures, the loading capacity and dispersity of Au nanocrystals are both improved. These magnetic microflowers present excellent catalytic efficiency and cycling performance in reduction of 4-nitrophenol to 4-aminophenol, which can be ascribed to the superior structure of catalyst. After 9 cycles, the activity of Fe₃O₄@SiO₂@γ-AlOOH@Au/PDA maintains as high as 97.3% due to the protection of PDA shell. In comparison to the spherical Fe₃O₄@SiO₂@Au/PDA, the as-prepared Fe₃O₄@SiO₂@γ-AlOOH@Au/PDA microflowers exhibit quicker catalytic dynamic. The concept of hierarchical nanostructure and penetrable PDA protective layer will be instructive for fabricating high-performance nanocatalysts.

1. Introduction

Due to their adjusting physicochemical properties, noble metals with tunable nanostructures have attracted much attentions in a wide range of applications, such as catalysis, sensors, imaging, biology, medicine, etc. [1–3]. Different from the bulk materials, noble metal nanocrystals exhibit superior performance in the catalytic fields which must be benefited from the small size, large specific surface areas, large amount of catalytic active pots and high exposure of crystal facets [4,5]. However, the aggregation of nanocatalysts in catalytic process and difficult recycling after reaction remained the key problems for developing noble metal nanocatalysts [6,7]. To this end, the noble metal nanocrystals were usually immobilized on the nanocarriers to improve the stability and catalytic activity [8–10]. During the past decades, various efforts have been conducted to explore high performance nanocarriers to

improve the utilization of noble metals [11,12]. Specifically, the core/shell structured nanocomposites are of great attractive in nanocatalysis because they can integrate different components together so as to achieve the synergistic enhancing performance [13–15].

Among them, the magnetic core/shell nanocarriers have received increasing interests because they can be easily separated from the reaction system by a simple remote magnetic recycling method [16–18]. Significant progress has been conducted to fabricate magnetic core–shell nanocatalysts owing to their special nanostructure and wonderful catalytic characteristics [19,20]. Han et al. synthesized Fe₃O₄/PANI/m-SiO₂ core–shell nanospheres as an effective carrier for nanocatalyst [21]. The noble metal nanoparticles could be fixed on the surface of PANI *via* redox reaction and the final hybrid nanocatalyst showed high stability and recyclability in the liquid-phase reaction. Recently, Yang et al. successfully prepared carbon dot (CD) modified Pd nanoparticles which

* Corresponding authors.
  E-mail addresses: jiangwq@ustc.edu.cn (W. Jiang), fql.good@hfut.edu.cn (Q. Fang), gongxl@ustc.edu.cn (X. Gong).
[1] The two authors contributed equally to this work.

were loaded on magnetic core–shell nanospheres [22]. The nanocomposites possessed superior catalytic performance in Knoevenagel condensation and Suzuki cross-coupling reaction due to the synergistic effect of different components. However, most of the reported magnetic core–shell nanomaterials possessed small surface area, which limited the loading capacity of noble metal nanocrystals and reduced the catalytic efficiency [23]. Therefore, it is essential to improve the carrying capacity of magnetic core/shell nanocomposites by introducing high surface area, large amount of active points, and tunable nanostructure.

Self-assembled hierarchical nanoarchitectures have attracted massive interests since this structure can avoid aggregation and increase the specific surface area [24–28]. Typically, AlOOH has been widely employed as a catalyst carrier [29–31] and adsorbent [32,33] due to the low cost, large specific surface area, high adsorption capacity and good solubility. It was found that the self-assembled γ-AlOOH hierarchical superstructures exhibited brilliant performance in the removal of Pb(II) and Hg(II) ions [34]. Nevertheless, the hydrophilic hierarchical γ-AlOOH was difficult to be separated from aqueous solution. To improve the reusability, magnetic $Fe_2O_3@AlO(OH)$ superstructure nanomaterial was prepared and it showed excellent adsorption performance for removing heavy metal ions [32]. Furthermore, $Fe_2O_3@AlO(OH)$ could be quickly separated from the reaction system by simply using a magnet. However, the application of the magnetic nanocomposites with hierarchical AlOOH surface as the nanocarrier for nanocatalysts is still rare. More importantly, the surface immobilized nanocrystals were very easily to be leached during the catalytic reaction [35]. Therefore, a penetrated protecting shell is required to improve the stability of the noble metal nanocatalysts. To this end, it is of special importance to develop novel proof-of-concept magnetic separable hierarchical nanocatalysts with enhancing activities and stability.

In this work, the $Fe_3O_4@SiO_2@\gamma$-AlOOH magnetic core–shell nanocomposites with hierarchical nanoarchitectures are synthesized for carrying Au nanocrystals with a PDA (polydopamine) protecting shell. The thickness of SiO_2 layer, surface modification of Fe_3O_4 core and urea concentration are adjusted and controlled to explore the optimum synthesis condition. The catalytic activities of the $Fe_3O_4@SiO_2@\gamma$-AlOOH@Au/PDA microflowers are tested by using the reduction of 4-nitrophenol to 4-aminophenol as the model reaction. Compared with $Fe_3O_4@SiO_2@Au/PDA$ microspheres, $Fe_3O_4@SiO_2@\gamma$-AlOOH@Au/PDA exhibits better catalytic activity and cyclability. The core–shell structure magnetic hierarchical nanocatalyst showed easy magnetic separation and recycling, high catalytic performance, and superior stability, thus it possesses great application potential in nanocatalysis.

2. Experimental section

2.1. Materials

Iron (III) chloride hexahydrate ($FeCl_3 \cdot 6H_2O$), diethylene glycol ($C_4H_{10}O_3$), sodium acetate ($C_2H_3O_2Na$), ploy (acrylic acid) (PAA, 1800), tetraethoxysilane (TEOS), ammonia solution ($NH_3 \cdot H_2O$), ethanol (EtOH), gold(III) chloride (HAuCl4), trihydroxymethyl aminomethane (Tris), hydrochloric acid (HCl), urea, aluminium nitrate (Al(NO_3)$_3 \cdot 9H_2O$), sodium borohydride ($NaBH_4$) and 4-nitrophenol were obtained from Sinopharm Chemical Reagent Co., Ltd. 3-hydroxytyramine hydrochloride (DA-HCl) was received from Aladdin. All reagents were used without further treatment and ultrapure water was used in all experiments.

2.2. Preparation of flower-like $Fe_3O_4@SiO_2@\gamma$-AlOOH@Au/PDA and $Fe_3O_4@SiO_2@Au/PDA$ microspheres

Firstly, $Fe_3O_4@SiO_2$ nanospheres were synthesized by the previously reported solvothermal method and modified Stöber reaction [36,37]. The thickness of SiO_2 shell was adjusted by the TEOS concentration. Then, $Fe_3O_4@SiO_2$ nanospheres were dispersed in 10 mL ethanol under

sonication. After that, 0.1872 g Al(NO_3)$_3 \cdot 9H_2O$, 1.3514 g urea and 10 mL water were introduced and mixed well. The homogeneous mixture was transferred into Teflon-lined stainless-steel autoclave and heated at 190 °C. After 24 h, the flower-like particles were separated by magnet and washed with water and ethanol. Finally, Au nanocrystals and PDA protective shell were prepared by *in situ* redox-oxidation polymerization method [38]. Typically, 60 μL $HAuCl_4$ and 40 mL DA-HCl Tris (1 mg/mL) solution were added into $Fe_3O_4@SiO_2@\gamma$-AlOOH ethanol dispersion (0.25 mg/mL) under ultrasonication. After 3 h reaction, the final products ($Fe_3O_4@SiO_2@\gamma$-AlOOH@Au/PDA) were collected by magnet and washed with ethanol and water.

Meanwhile, the $Fe_3O_4@SiO_2@Au/PDA$ microspheres were obtained *via* a similar method. Briefly, 60 μL $HAuCl_4$ and 40 mL DA-HCl Tris (1 mg/mL) solution were added into $Fe_3O_4@SiO_2$ ethanol dispersion (0.25 mg/mL) under ultrasonication. After reacting for 3 h, the final products were collected by magnet and washed with ethanol and water.

2.3. Catalytic properties of as-prepared catalysts on the reduction of 4-nitrophenol

The catalytic activity of $Fe_3O_4@SiO_2@\gamma$-AlOOH@Au/PDA was evaluated by the reduction of 4-nitrophenol with $NaBH_4$. Typically, 2 mg $Fe_3O_4@SiO_2@\gamma$-AlOOH@Au/PDA was dispersed into 50 mL 4-nitrophenol aqueous solution (1×10^{-4} M), and then 40 mg $NaBH_4$ was added to start the reaction. The conversion process of 4-nitrophenol was tested by UV–Vis spectrophotometer. As a contrast, 2 mg $Fe_3O_4@SiO_2@Au/PDA$ microspheres were also used to catalyze the reduction of 4-nitrophenol with the same experiment condition. Furthermore, the reusability of $Fe_3O_4@SiO_2@\gamma$-AlOOH@Au/PDA was evaluated in the aforementioned reaction system. After each cycle, $Fe_3O_4@SiO_2@\gamma$-AlOOH@Au/PDA was collected and reused for the next cycle.

2.4. Characterization

The morphologies and inner structure of the samples were observed under transmission electron microscopy (TEM, H-7650). The x-ray diffractometer (Smartlab, Rigaku, Japan) was used to record the X-ray diffraction (XRD) pattern of the products. X-ray photoelectron spectroscopy (XPS) results of the products were detected on the X-ray photoelectron spectrophotometer (Thermo ESCALAB 250). The hysteresis loops were operated on a magnetometer (SQUID-VSM Quantum Design Co., America) at room temperature.

3. Results and discussion

3.1. Synthesis and characterization of $Fe_3O_4@SiO_2@\gamma$-AlOOH@Au/PDA

The morphology and nanostructure of $Fe_3O_4@SiO_2@\gamma$-AlOOH@Au/PDA are characterized by TEM. As shown in Fig. 1a, the $Fe_3O_4@SiO_2@\gamma$-AlOOH@Au/PDA microflowers are uniformly dispersed on the carbon supported copper grid without apparent aggregation. $Fe_3O_4@SiO_2@\gamma$-AlOOH@Au/PDA possesses unique hierarchical core–shell structure. The average diameter of microflowers is approximately 600 nm. Fig. 1b clearly exhibits the inner nanostructure of $Fe_3O_4@SiO_2@\gamma$-AlOOH@Au/PDA microflower, in which center nanosphere is magnetic component (Fe_3O_4) and surrounded part on the surface of Fe_3O_4 is SiO_2 shell ($Fe_3O_4@SiO_2$). Moreover, it can be observed that there are some cavities between Fe_3O_4 core and SiO_2 shell. The curved and irregular sheets in the periphery of microflower are γ-AlOOH nanosheets with sizes of about 100–300 nm. From the high magnification TEM images (Fig. 1c and d), one can find that the SiO_2 layer is closely connected with γ-AlOOH nanosheets to form a stable flower-like structure. The γ-AlOOH nanosheets assemble on the SiO_2 surface to form hierarchical architectures which significantly increase the surface area of nanocomposite and provide sufficient carrying sites for noble metal nanocrystals. Au
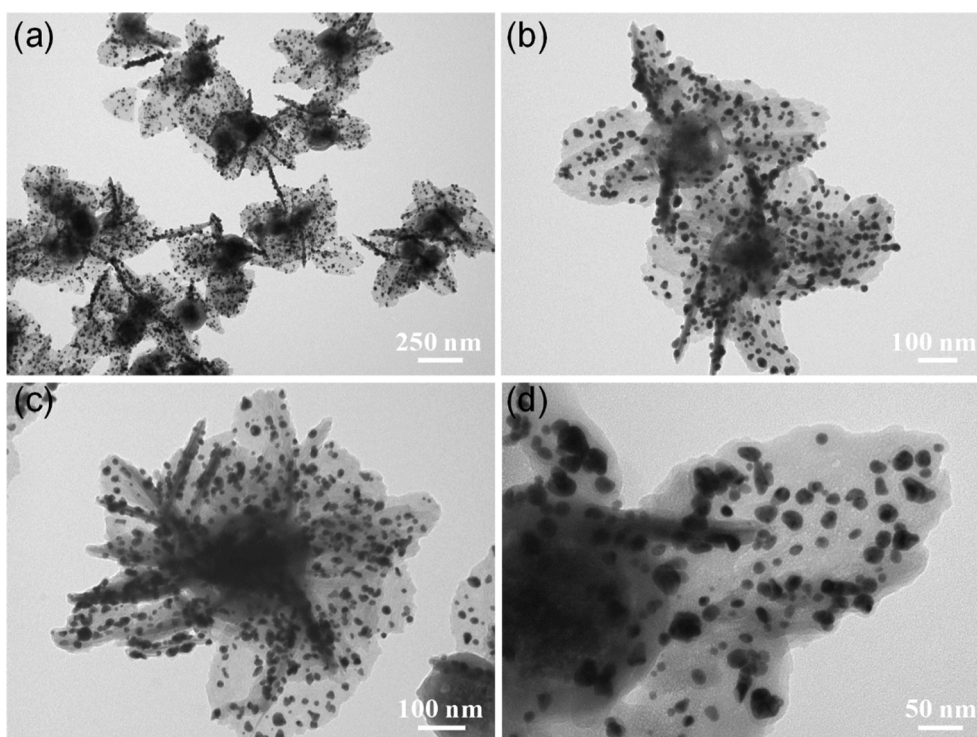
Fig. 1. TEM images of the Fe$_3$O$_4$@SiO$_2$@γ-AlOOH@Au/PDA with different magnification.
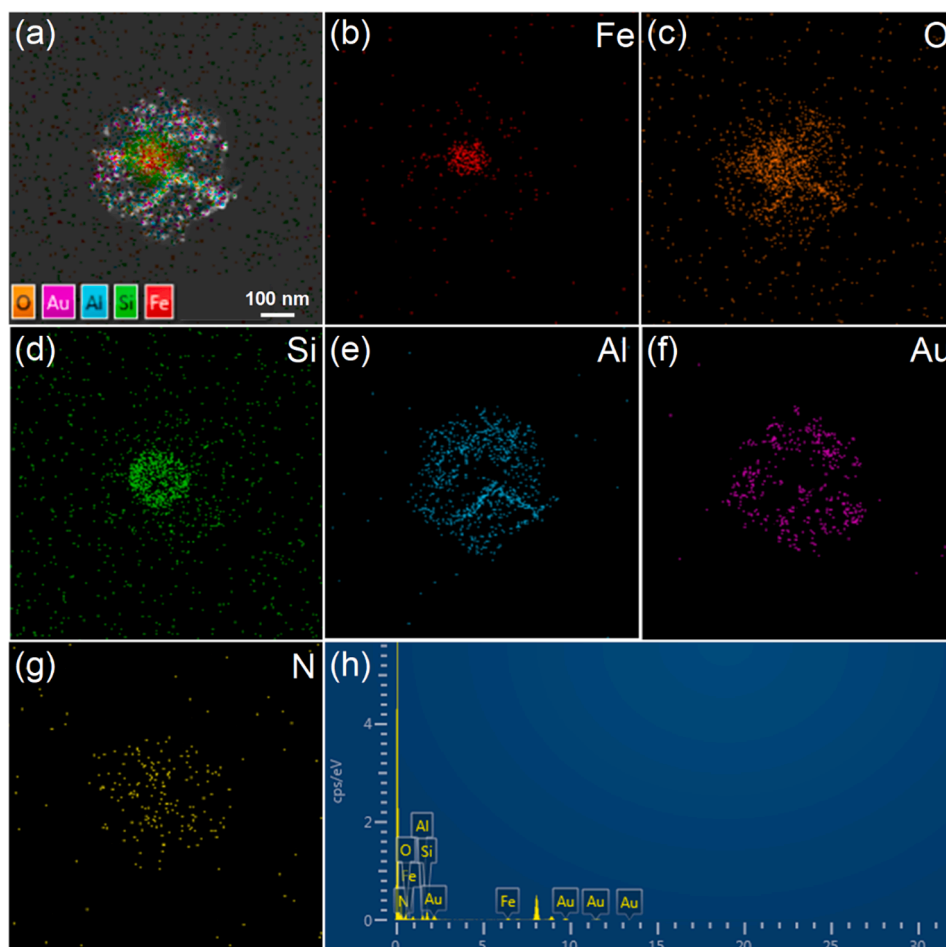
Fig. 2. Elemental mapping images (a–g) and EDS spectrum (h) of Fe$_3$O$_4$@SiO$_2$@γ-AlOOH@Au/PDA.

nanocrystals are uniformly dispersed on the surface of γ-AlOOH nanosheets (Fig. 1c). By measuring the size of Au nanocrystals in high magnification TEM image (Fig. 1d), the average diameter is calculated to be about 14 nm. Here, the Au nanocrystals are encapsulated by a thin layer of PDA polymer during the *in situ* redox-oxidation polymerization method. It is difficult to observe the PDA layer from TEM images because the contrast of thin PDA layer is very weak.

To further investigate the formation of Fe₃O₄@SiO₂@γ-AlOOH@Au/PDA, the elemental mapping images and EDS spectrum were conducted. The EDS spectrum shows that the Fe₃O₄@SiO₂@γ-AlOOH@Au/PDA contains Fe, O, Si, Al, Au and N elements. Elemental mapping images exhibit the distribution of every element in an individual Fe₃O₄@SiO₂@γ-AlOOH@Au/PDA. As shown in Fig. 2b, the Fe element is distributed in central area, which is derived from the magnetic Fe₃O₄ core. The shape of Si element is a circle and the diameter of Si signal is larger than that of Fe, indicating the SiO₂ layer uniformly wraps around the Fe₃O₄ core. Al and O elements occupied in the Fe₃O₄@SiO₂@γ-AlOOH@Au/PDA mapping area just like a flower. Furthermore, the intensity of O in center is higher than that in the periphery, which is ascribed to the core–shell structure of Fe₃O₄@SiO₂@γ-AlOOH@Au/PDA. The distribution of Au is similar with Al element because Au nanocrystals are dispersed on the surface of γ-AlOOH nanosheets. The detected N element also shows a relatively weak intensity, which must be attributed to the thin PDA layer and low N content in PDA. The elemental mapping image and EDS spectrum analysis further reveal the Fe₃O₄@SiO₂@γ-AlOOH@Au/PDA product presents a hierarchical core–shell structure and the corresponding element distribution is consistent with the composition of each part.

Magnetic properties play an important role in the recovery and reuse of the catalyst. The magnetic properties of each sample were examined by a magnetometer at room temperature and the corresponding M−H curves are shown in Fig. 3. With increasing of the magnetic field, the magnetization of the product is increased and reached to the saturation eventually. In addition, the magnetization curve is essentially coincident with the demagnetization curve, indicating that all products are equipped with typical superparamagnetism. The superior magnetic properties are beneficial to recycle the as-prepares catalyst. The saturation magnetizations of Fe₃O₄, Fe₃O₄@SiO₂, Fe₃O₄@SiO₂@γ-AlOOH and Fe₃O₄@SiO₂@γ-AlOOH@Au/PDA are 65.8, 19.8, 17.9, and 15.5 emu/g, respectively. The introduction of non-magnetic components leads to the reduction of saturation magnetizations of products. But the magnetic sensitivity of the final sample (Fe₃O₄@SiO₂@γ-AlOOH@Au/PDA) is sufficient to separate from the reaction system using a magnet. The illustrated diagram of the magnetic separation process sufficiently supports the above analysis (inset of Fig. 3)

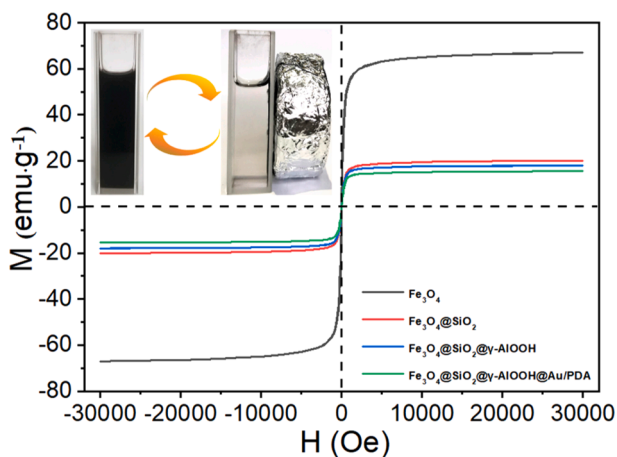The crystalline structures of each product were tested by X-ray

diffractometer (Fig. 4a). From the XRD pattern of Fe₃O₄, the diffraction peaks at 2θ of 30.1°, 35.5°, 43.0°, 56.9° and 62.6° are corresponding to the (220), (311), (400), (422), (511) and (440) crystalline planes of Fe₃O₄, respectively. This information manifests the face-centered cubic structure of Fe₃O₄. After the SiO₂ is coated on the Fe₃O₄, there is no new peak in the XRD curve of Fe₃O₄@SiO₂, which is attributed to an amorphous structure of SiO₂. In comparison to the XRD patterns of Fe₃O₄@SiO₂, four additional diffraction peaks are found at 14.6°, 28.2°, 38.6° and 49.3° for Fe₃O₄@SiO₂@γ-AlOOH. According to the JCPDS card 21-1307, the new diffraction peaks represent the Bragg reflections from the (020), (120), (031), and (200) crystal planes of the orthorhombic γ-AlOOH, respectively [39]. After the simultaneous loading of Au nanocrystals and PDA, the peaks at 2θ = 38°, 44.7° and 64.7° are related to the (111), (200) and (220) crystal planes of Au, which demonstrates the presence of Au nanocrystals. Because the amorphous structural PDA has no crystal plane diffraction, it is difficult to prove the existence of PDA by XRD pattern.

In order to further testify the formation of core–shell structure, XPS was performed to detect the surface elements of each product. As exhibited in Fig. 4b, the characteristic peaks of C 1s, O 1s, Fe 3p and Fe 2p are presented in the XPS of Fe₃O₄. Obviously, the C 1 s signal is originated from the residual reagent. In the XPS of Fe₃O₄@SiO₂, it can be observed that the characteristic peaks of Si 2p are located at 157 eV and 107 eV, while the signal peaks of Fe 3p and Fe 2p disappear. The XPS analysis reveals that the SiO₂ is wrapped on Fe₃O₄ to form a typical core–shell structure and the thickness of SiO₂ is more than 10 nm, thus the Fe element cannot be detected. Similarly, as soon as the γ-AlOOH nanosheets are assembled to form a flower-like structure on the surface of Fe₃O₄@SiO₂, new peaks corresponding to Al 2s and Al 2p are appeared. By observing carefully at the XPS curve of Fe₃O₄@SiO₂@γ-AlOOH, it can be found that the Si 2p signal still exists and the intensity is weak. The reason is that the γ-AlOOH nanosheets are immobilized on the surface of Fe₃O₄@SiO₂ instead of forming uniform shell. For the target product, the typical peaks of Au 4f and Au 4d can be discovered except for O 1s, C 1s, Si 2p, Al 2s and Al 2p signals, which demonstrates that Au nanocrystals are fixed on the surface of γ-AlOOH. In addition, the characteristic N element in PDA (N 1s 400 eV) is also detected, illustrating the presence of PDA. Here, the thickness of PDA layer is very thin, which is less than the detection depth of XPS of 10 nm. Hence, the Au signal can be clearly observed in the final product.

The synthesis procedure sketches of Fe₃O₄@SiO₂@γ-AlOOH@Au/PDA are stated in Fig. 4a. Firstly, the monodispersed Fe₃O₄ nanospheres are synthesized by hydrothermal method and equably coated with SiO₂ layer through TEOS hydrolysis in alkaline environment. As-prepared Fe₃O₄ particles possess spherical morphology with an average size of about 120 nm (Fig. 5b). Fe₃O₄ nanospheres exhibit cluster-like structure because they consist of numerous small nanocrystals (Fig. 5c). As shown in Fig. 5d and e, monodispersed Fe₃O₄@SiO₂ nanoparticles present typical core–shell structure. The Fe₃O₄ core is located in the center and the surrounding SiO₂ shell is dense and uniform with the thickness of about 75 nm. The decoration of SiO₂ layer not only protects the Fe₃O₄ core but also benefits for the formation of γ-AlOOH flower-like structure. Through solvothermal reaction, γ-AlOOH nanosheets are immobilized on the surface of Fe₃O₄@SiO₂ and assembled to a flower-like structure. As Fig. 5f shows that Fe₃O₄@SiO₂@γ-AlOOH composites are homogeneous and dispersive. Owing to the formation of γ-AlOOH hierarchical architectures, the particles size increases significantly and the average diameter of Fe₃O₄@SiO₂@γ-AlOOH is about 600 nm. From the high magnification TEM image (Fig. 5g), it is obvious that there is cavity space between Fe₃O₄ core and SiO₂ shell, indicating that the SiO₂ is etched during the formation of γ-AlOOH. Finally, the Au nanocrystals, which are coated with a thin PDA layer *via* one-step *in-situ* redox-oxidation polymerization reaction, are attached on the surface of γ-AlOOH. The TEM images of Fe₃O₄@SiO₂@γ-AlOOH@Au/PDA (Fig. 5h and i) clearly reveal that dense Au nanocrystals are tightly immobilized on the surface of γ-AlOOH nanosheets. As-prepared

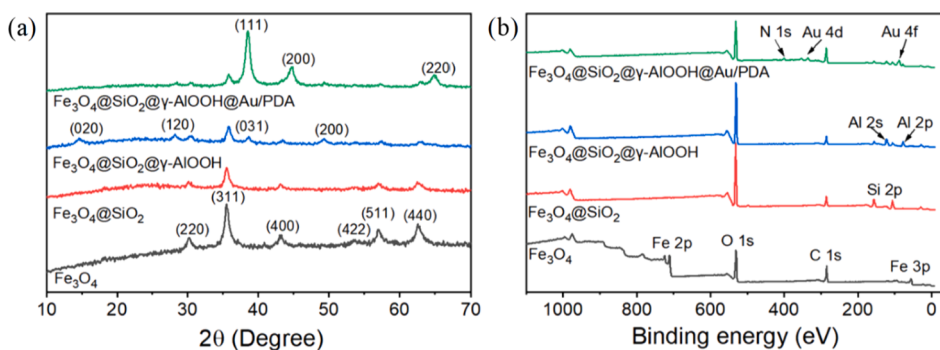**Fig. 3.** M−H curves of the samples obtained from each step and the inset is the illustration of the magnetic separation process.

Fig. 4. XRD pattern (a) and XPS (b) of the samples obtained from each step.
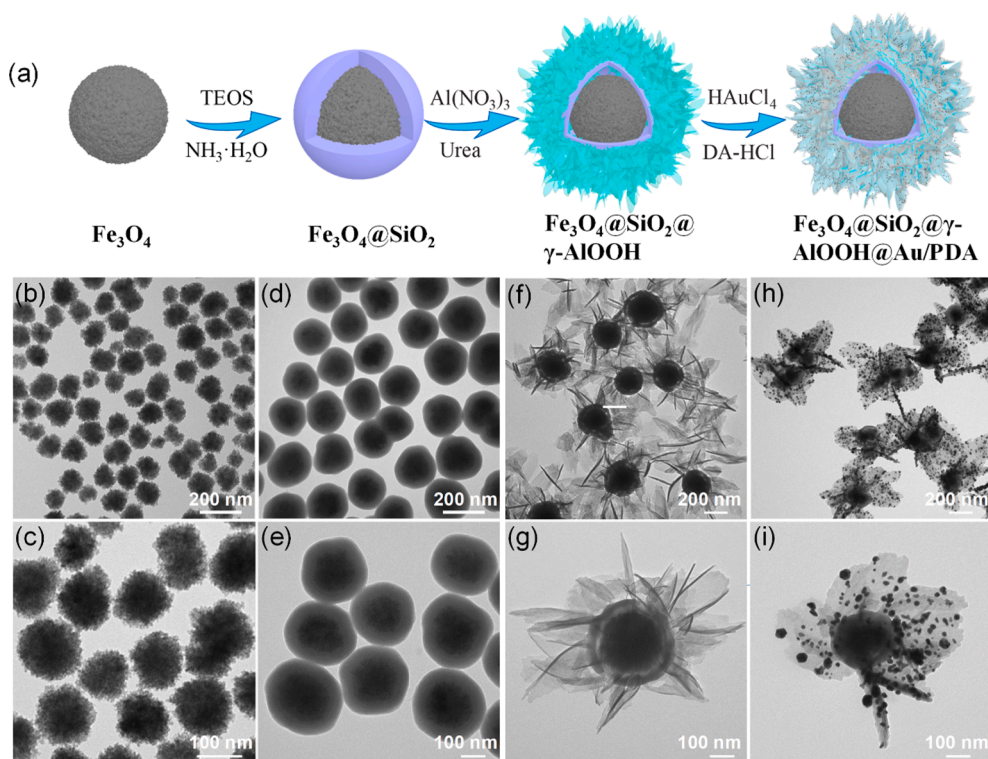
Fig. 5. Synthesis procedure sketches of Fe$_3$O$_4$@SiO$_2$@γ-AlOOH@Au/PDA (a), TEM image of Fe$_3$O$_4$ (b, c), Fe$_3$O$_4$@SiO$_2$ (d, e), Fe$_3$O$_4$@SiO$_2$@γ-AlOOH (f, g), Fe$_3$O$_4$@SiO$_2$@γ-AlOOH@Au/PDA (h, i).

Fe$_3$O$_4$@SiO$_2$@γ-AlOOH@Au/PDA maintains flower-like morphology without structural collapse and obvious agglomeration.

In order to explore the formation mechanism of flower-like Fe$_3$O$_4$@SiO$_2$@γ-AlOOH, the preparation process is analyzed in detail. In the synthesis process of Fe$_3$O$_4$@SiO$_2$@γ-AlOOH, the urea and aluminium nitrate reagents are dissolved into the mixed solution that contains Fe$_3$O$_4$@SiO$_2$ nanospheres, water and ethanol. Then, the mixture is transferred into reaction kettle and heated at 190 °C for 24 h. In the hydrothermal reaction, the urea is decomposed to form alkaline conditions and the aluminate anions are generated in a sufficient OH$^-$ environment. However, at high temperatures, aluminate anions are converted into Al(OH)$_3$ colloids. The newly-formed Al(OH)$_3$ colloids are unstable that will further dehydrate to form γ-AlOOH[39]. In the alkaline conditions, the Si—O bond of SiO$_2$ will break and consume the OH$^-$ in the reaction system, which further promotes the formation of γ-AlOOH. Above analyses indicate that the formation of γ-AlOOH nanosheets and etching of SiO$_2$ complement are simultaneously taken place. So, the SiO$_2$ layer can closely connect with γ-AlOOH nanosheets to form a stable flower-like structure. The presence of γ-AlOOH is beneficial to form

stable Fe$_3$O$_4$@SiO$_2$@γ-AlOOH@Au/PDA magnetic microflower.

Fig. 6a–c exhibits the effects of the thickness of SiO$_2$ shell on the morphology of Fe$_3$O$_4$@SiO$_2$@γ-AlOOH. When the thickness of SiO$_2$ shell is thin (Fe$_3$O$_4$@SiO$_2$ is obtained through the sol–gel process with 0.1 mL TEOS), Fe$_3$O$_4$@SiO$_2$@γ-AlOOH is formed with incomplete flower-like structure. There are partially independent core particles in the samples and only a few γ-AlOOH nanosheets are immobilized on the surface of core. As shown in Fig. 6a, the SiO$_2$ shell is completely etched in the reaction. Owing to the weak interaction between Fe$_3$O$_4$ and γ-AlOOH, it is difficult to constitute ideal hierarchical nanoarchitectures with abundant γ-AlOOH nanosheets. With the thickness of SiO$_2$ shell rising (Fe$_3$O$_4$@SiO$_2$ is obtained through the sol–gel process with 0.2 mL TEOS), massive γ-AlOOH nanosheets are generated and adhered to the Fe$_3$O$_4$@SiO$_2$ core for the assembly of flower-like Fe$_3$O$_4$@SiO$_2$@γ-AlOOH (Fig. 6b). In Fig. 6b, it is distinct that the SiO$_2$ shell remains but there is cavity space between the Fe$_3$O$_4$ and SiO$_2$. This phenomena infers that SiO$_2$ shell is etched from interior to external in the hydrothermal process, which is ascribe to the loose SiO$_2$ framework at the interface of Fe$_3$O$_4$ and SiO$_2$. Further increasing the thickness of SiO$_2$ shell
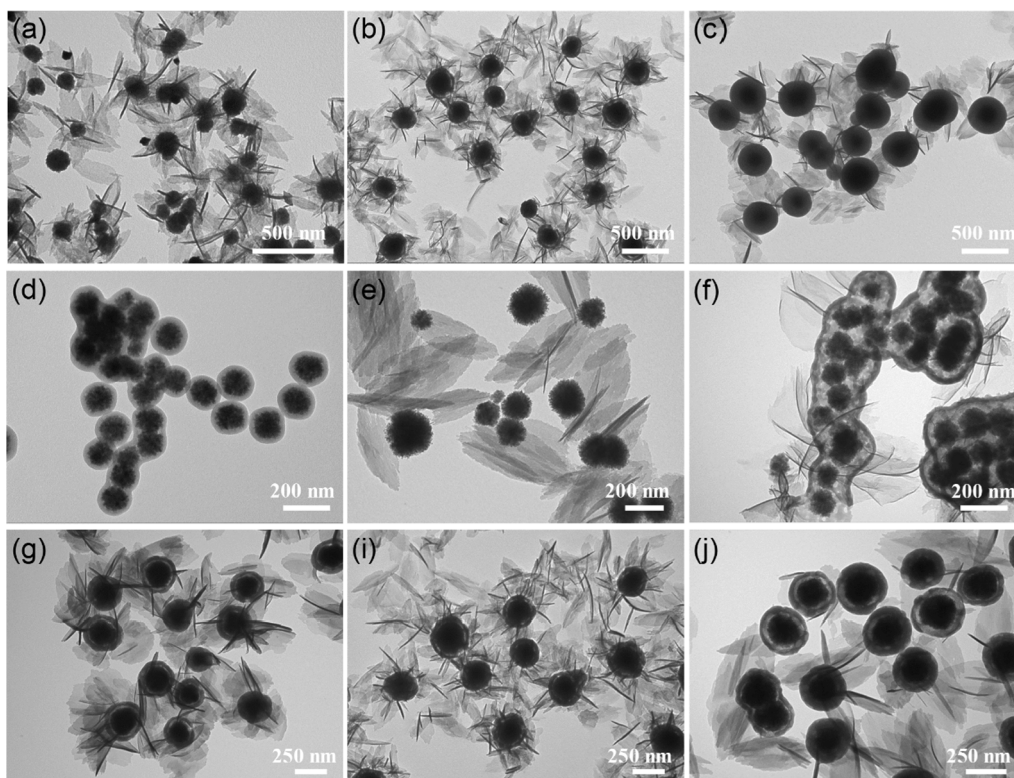
Fig. 6. TEM image of Fe₃O₄@SiO₂@γ-AlOOH with different thickness of shell Fe₃O₄@SiO₂ core: 0.1 mL TEOS (a), 0.2 mL TEOS (b), 0.4 mL TEOS (c); TEM image of Fe₃O₄@RF@γ-AlOOH (d), Fe₃O₄@PDA@γ-AlOOH (e), Fe₃O₄@SiO₂/CTAB@γ-AlOOH (f); TEM image of Fe₃O₄@SiO₂@γ-AlOOH with different urea concentration: 0.6757 g (g), 1.3514 g (h), 2.0271 g (i).

(Fe₃O₄@SiO₂ is obtained through the sol–gel process with 0.4 mL TEOS), the SiO₂ shell still exists without obvious cavity space after the reaction (Fig. 6c). This Fe₃O₄@SiO₂ nanosphere has thick, dense and solid SiO₂ shell, which is not good for the internal etching. Additionally, the number of γ-AlOOH that on the periphery of Fe₃O₄@SiO₂ is small and the size is obviously reduced. Therefore, the appropriate thickness of SiO₂ layer is beneficial to the formation of γ-AlOOH hierarchical nanoarchitectures.

To further confirm that the SiO₂ layer is conducive to the construction of flower-like structure, the Fe₃O₄@RF@γ-AlOOH and Fe₃O₄@PDA@γ-AlOOH were synthesized by a similar method (the RF is represents the resorcinol/formaldehyde resin layer). TEM images in Fig. 6d and e show that Fe₃O₄@RF@γ-AlOOH and Fe₃O₄@PDA@γ-AlOOH are both failed to form desired hierarchical structure. If the Fe₃O₄@SiO₂/CTAB as core nanomaterial, as-prepared Fe₃O₄@SiO₂/CTAB@γ-AlOOH owns visible cavity space, while the number of γ-AlOOH nanosheets is small. The addition of CTAB results in a serious agglomeration of Fe₃O₄@SiO₂/CTAB, which causes the significantly reduced dispersion of Fe₃O₄@SiO₂/CTAB@γ-AlOOH.

Alkaline environment plays a key role in the generation of flower-like Fe₃O₄@SiO₂@γ-AlOOH and cavity space. Meanwhile, the effect of urea concentration on the morphology of Fe₃O₄@SiO₂@γ-AlOOH is investigated. As exhibited in Fig. 6g–i, the cavity space in Fe₃O₄@SiO₂@γ-AlOOH increases significantly with the increasing of urea concentration. Whereas, excessive concentration of urea is against the growth of γ-AlOOH nanosheets (Fig. 6i). Therefore, the ideal γ-AlOOH hierarchical nanoarchitectures only can be obtained under optimized conditions, utilizing the synergy of alkaline etching and hydrolysis reaction.

Flower-like Fe₃O₄@SiO₂@γ-AlOOH provides sufficient active sites for the loading of Au nanocrystals. The concentration of HAuCl₄ severely affects the final product. After introducing the dopamine, the reductive oxidation and polymerization reactions occur simultaneously to form Au

and PDA nucleation. When the HAuCl₄ concentration is low, the relative concentration of dopamine is high. PDA quickly adsorbs on the surface of Au nanocrystals to form Au/PDA nanoparticles, due to the Oswald ripening phenomenon. Owing to the low concentration of HAuCl₄, there are a few Au/PDA nanoparticles adhered to the surface of γ-AlOOH nanosheets (Fig. 7a). With increasing of the HAuCl₄ concentration, Au/PDA nucleus are increased and more Au/PDA nucleus are attached to the γ-AlOOH nanosheets. Further enhancing the concentration of HAuCl₄, the number of Au/PDA nucleus is increased markedly and Au/PDA nucleus are uniformly dispersed on the γ-AlOOH nanosheets without obvious agglomerations (Fig. 7c and d). Au nanocrystals are uniformly dispersed on the surface of the carrier, which can be attributed to three factors. Firstly, flower-like Fe₃O₄@SiO₂@γ-AlOOH with high specific surface area that provides abundant active sites for Au nanocrystals. Secondly, the Au/PDA nucleuses are generated *via* one-step approach, which effectively inhibits the agglomeration of Au nanocrystals. Finally, PDA is easy to adhere to the surface of organic or inorganic substrates, which further improves the loading rate and stability of noble metal nanocrystals. Moreover, Fig. 7e–h present that all Fe₃O₄@SiO₂@γ-AlOOH@Au/PDA are monodispersed, which indicates this covering method is universal.

3.2. The catalytic properties of Fe₃O₄@SiO₂@γ-AlOOH@Au/PDA

The 4-nitrophenol is a common organic pollutant which can cause various diseases for the humans and animals because of its toxicity, degradation-resistant and bioaccumulation. It is necessary to develop efficient method to solve the organic pollutant in the environment. Furthermore, in the presence of catalyst, the 4-nitriphenol can be reduce to 4-aminophnol with low toxicity and the conversion process can be recorded by UV–vis spectrophotometer. Therefore, the reduction of 4-nitrophenol to 4-aminophenol is chosen as the model reaction for evaluating the catalytic activities of Fe₃O₄@SiO₂@γ-AlOOH@Au/PDA.

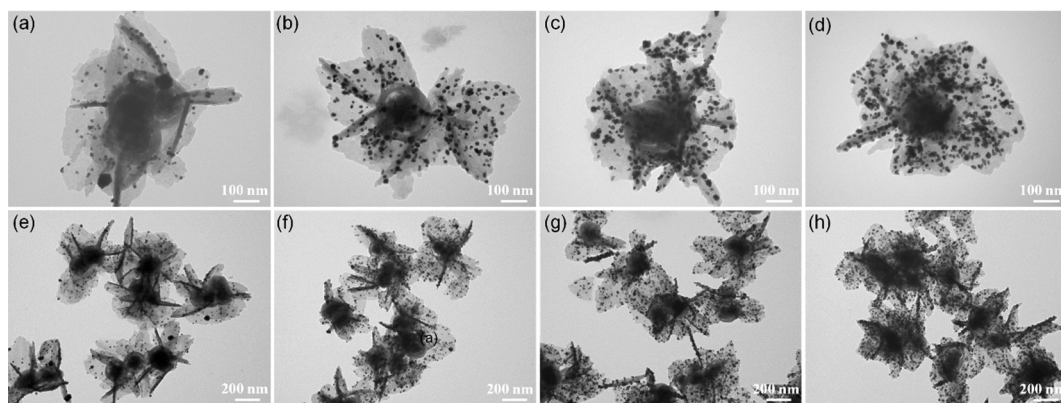**Fig. 7.** TEM images of Fe$_3$O$_4$@SiO$_2$@γ-AlOOH@Au/PDA prepared with different concentration of HAuCl$_4$: 20 μL (a, e), 40 μL (b, f), 60 μL (c, g), 80 μL HAuCl$_4$ (d, h).

The mechanism of 4-nitrophenol reduction by Fe$_3$O$_4$@SiO$_2$@γ-AlOO-H@Au/PDA is mainly composed of three steps. Firstly, 4-nitrophenate ion intermediate are adsorbed on the surface of Au particles, and Au provides a reaction site, and then realize the electron transport and atom exchange on the surface of Au nanocrystals. The Au nanocrystals catalyze sodium borohydride to generate free hydrogen, and the free hydrogen attacks the —NO$_2$ group on the para position of 4-nitrophenol, and finally generates 4-aminophenol.
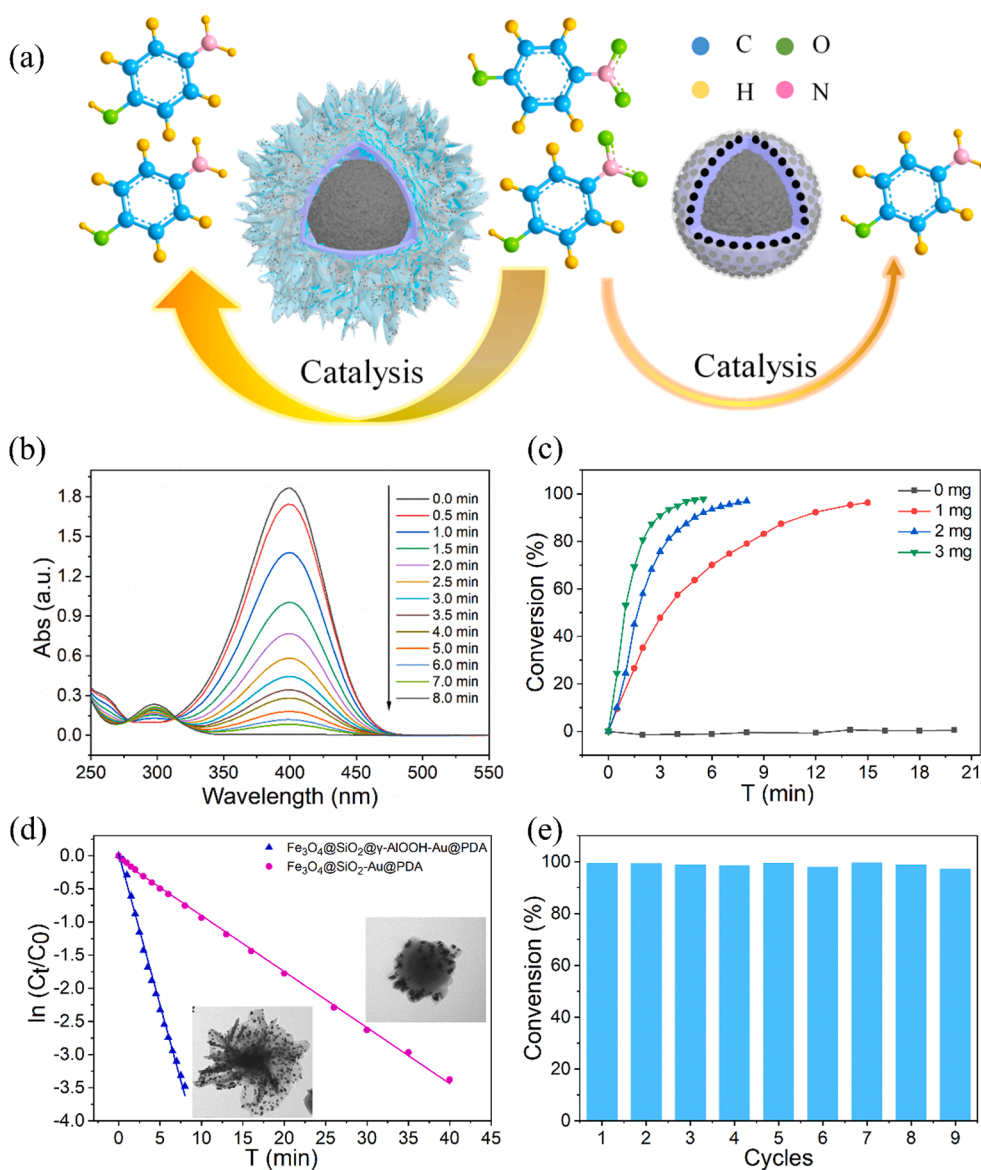

Fig. 8. The schematic of 4-nitrophenol reduction catalyzed by Fe$_3$O$_4$@SiO$_2$@γ-AlOOH@Au/PDA and Fe$_3$O$_4$@SiO$_2$@Au/PDA (a), UV–vis spectra of the 4-nitrophenol reduction that catalyzed by 2 mg Fe$_3$O$_4$@SiO$_2$@γ-AlOOH@Au/PDA catalyst (b), plot of conversion (%) of 4-nitrophenol versus time (t, min) at different concentrations of Fe$_3$O$_4$@SiO$_2$@γ-AlOOH@Au/PDA (c), the linear relationship of ln(C$_t$/C$_0$) versus reaction time (t), inserted images are TEM images of Fe$_3$O$_4$@SiO$_2$@γ-AlOOH@Au/PDA and Fe$_3$O$_4$@SiO$_2$@Au/PDA, respectively (d), conversion of 4-nitrophenol in 9 cycles that catalyzed by Fe$_3$O$_4$@SiO$_2$@γ-AlOOH@Au/PDA (e).

Fig. 8a schematically show that the 4-nitrophenol can be translated into 4-aminophenol in presence of catalyst. In the reaction, the 4-nitrophenol can react with $NaBH_4$ quickly to generate 4-nitrophenate ion intermediate that has a characteristic absorption peak at 400 nm. As shown in Fig. 8b, the intensity of absorption peak at 400 nm gradually decreases with the extension of the reaction time, while new peaks at 300 nm are appeared with enhanced intensity. The peak at 300 nm is the characteristic peak of 4-aminophenol, indicating that $Fe_3O_4@SiO_2@\gamma$-AlOOH@Au/PDA can catalyze 4-nitrophenol to 4-aminophenol and the reaction is completed within 8 min by using 2 mg nanocatalysts. With increasing the content of $Fe_3O_4@SiO_2@\gamma$-AlOOH@Au/PDA, the reaction time is shortened sharply (Fig. 8c). For comparison, the conversion rate of 4-nitrophenol is close to 0 without $Fe_3O_4@SiO_2@\gamma$-AlOOH@Au/PDA, which illustrate that the 4-nitrophenol reduction is not spontaneous. The reaction rate slowly decreases over time, illustrating that the reaction follows the pseudo-first-order kinetics.

In order to prove that substrates with high surface area is beneficial to enhance the properties of catalyst, $Fe_3O_4@SiO_2@Au/PDA$ nanospheres are prepared and its catalytic performance is studied. The linear relationship between $\ln(C_t/C_0)$ and reaction time (T) is shown in Fig. 8c, where C_t and C_0 represent the concentration of 4-nitrophenol at t and 0 min, respectively. The rate constants (k) are calculated to be 0.458 min^{-1} and 0.085 min^{-1} for $Fe_3O_4@SiO_2@\gamma$-AlOOH@Au/PDA and $Fe_3O_4@SiO_2@Au/PDA$, respectively. It is apparent that the catalytic efficiency of $Fe_3O_4@SiO_2@\gamma$-AlOOH@Au/PDA is better than that of $Fe_3O_4@SiO_2@Au/PDA$. Compared with $Fe_3O_4@SiO_2@Au/PDA$, it can be observed that more Au nanocrystals are immobilized on the surface of $Fe_3O_4@SiO_2@\gamma$-AlOOH@Au/PDA and the size Au nanocrystals is smaller (inserted images in Fig. 8c). The small surface area of $Fe_3O_4@SiO_2$ causes the aggregation of partly Au nanocrystals in $Fe_3O_4@SiO_2@Au/PDA$. In general, high surface area of substrates is good for the immobilization of more active particles, with further improving the efficiency of the catalyst.

Simultaneously, the recyclability is one of important parameters for catalyst to estimate its property. $Fe_3O_4@SiO_2@\gamma$-AlOOH@Au/PDA equipped with magnetic core can be easily recovered by a magnet. Moreover, the thin PDA layer protects Au nanocrystals from leaching during the catalytic cycle. As shown in Fig. 8d, no significant change in catalytic activity is discovered. After 9 cycles, the conversion of 4-nitrophenol is still as high as 97.3%. A series of catalytic experiments demonstrate that $Fe_3O_4@SiO_2@\gamma$-AlOOH@Au/PDA microspheres not only possesses high catalytic efficiency, but also has good stability.

4. Conclusions

In this work, a PDA-confined-Au-nanocrystals assembled on the hierarchical surface of $Fe_3O_4@SiO_2@\gamma$-AlOOH microflower has been developed as a proof-of-concept magnetic separable nanocatalyst. The loading capacity and dispersity of Au nanocrystals are both high because of the high surface area of $Fe_3O_4@SiO_2@\gamma$-AlOOH hierarchical nanoarchitectures. Since the high loading the $Fe_3O_4@SiO_2@\gamma$-AlOOH@Au/PDA microflowers exhibited quicker catalytic dynamic than the spherical $Fe_3O_4@SiO_2@Au/PDA$. The product exhibited wonderful activity of 97.3% after 9 cycle reaction, which must be responded for the protection of the external PDA shell. Moreover, $Fe_3O_4@SiO_2@\gamma$-AlOOH@Au/PDA microflowers can be easily collected by applying the magnetic field thus shows an easy separation performance. Here, the PDA-confined-Au-nanocrystals hybrid shell was achieved by a simple redox-oxidation polymerization reaction between the $HAuCl_4$ and dopamine, which simplifies the synthesis steps and reduces the loss of noble metal in the preparation process. This research work provides a concept for constructing high-performance magnetically separable nanocatalysts.

CRediT authorship contribution statement

Linfeng Bai: Investigation, Writing - original draft, Methodology,

Visualization. **Kezhu Xu:** Investigation, Writing - original draft, Formal analysis. **Wanquan Jiang:** Investigation, Methodology, Data curation. **Min Sang:** Formal analysis, Writing - review & editing, Data curation. **Qunling Fang:** Visualization, Methodology, Software. **Shouhu Xuan:** Methodology, Investigation, Writing - review & editing. **Xinglong Gong:** Resources, Supervision, Project administration, Funding acquisition.

Declaration of Competing Interest

The authors declare that they have no known competing financial interests or personal relationships that could have appeared to influence the work reported in this paper.

Acknowledgement

References

[1] T. Thai-Hoa, N. Thanh-Dinh, Controlled growth of uniform noble metal nanocrystals: aqueous-based synthesis and some applications in biomedicine, Colloid. Surf. B 88 (2011) 1–22.

[2] S.V.P. Vattikuti, P.C. Nagajyothi, K.C. Devarayapalli, K. Yoo, N.D. Nam, J. Shim, Hybrid Ag/MoS_2 nanosheets for efficient electrocatalytic oxygen reduction, Appl. Surf. Sci. 526 (2020) 146751.

[3] A.R. Woldu, From low to high-index facets of noble metal nanocrystals: a way forward to enhance the performance of electrochemical CO_2 reduction, Nanoscale 12 (2020) 8626.

[4] P. Ribao, J. Corredor, M.J. Rivero, I. Ortiz, Role of reactive oxygen species on the activity of noble metal-doped TiO_2 photocatalysts, J. Hazard. Mater. 372 (2019) 45–51.

[5] Y.S. Song, Y.S. Peng, N.V. Long, Z.R. Huang, Y. Yang, Multifunctional self-assembly 3D Ag/g-C_3N_4/RGO aerogel as highly efficient adsorbent and photocatalyst for R6G removal from wastewater, Appl. Surf. Sci. 148534 (2020).

[6] M. Guo, J. He, Y. Li, S. Ma, X. Sun, One-step synthesis of hollow porous gold nanoparticles with tunableparticle size for the reduction of 4-nitrophenol, J. Hazard. Mater. 310 (2016) 89–97.

[7] J.F. Zhang, Q.L. Fang, J.Y. Duan, H.M. Xu, H.J. Xu, S.H. Xuan, Magnetically separable nanocatalyst with the Fe_3O_4 core and polydopamine-sandwiched Au nanocrystal shell, Langmuir 34 (2018) 4298–4306.

[8] J.Y. Duan, L.F. Bai, K.Z. Xu, Q.L. Fang, Y.H. Sun, H.J. Xu, K.C. Leung, S.H. Xuan, Polydopamine protected hollow nanosphere with AuAg-nanoframe-core@ Carbon@AuAg-nanocrystals-satellite hybrid nanostructure (AuAg@C@AuAg/ PDA) for enhancing nanocatalysis, J. Hazard. Mater. 384 (2020).

[9] M. Zhang, Y. Ling, L. Liu, J. Xu, J. Li, Q. Fang, Carbon supported PdNi alloy nanoparticles on SiO_2 nanocages with enhanced catalytic performance, Inorg. Chem. Front. 7 (2020) 3081–3091.

[10] C.Z. Wang, J. Ding, G.F. Zhao, T. Deng, Y. Liu, Y. Lu, Microfibrous-structured Pd/ alooh/al-fiber for co coupling to dimethyl oxalate: effect of morphology of alooh nanosheet endogenously grown on al-fiber, ACS Appl. Mater. Interfaces 9 (2017) 9795–9804.

[11] Y. Fu, P. Xu, D. Huang, G. Zeng, C. Lai, L. Qin, B. Li, J. He, H. Yi, M. Cheng, C. Zhang, Au nanoparticles decorated on activated coke via a facile preparation for efficient catalytic reduction of nitrophenols and azo dyes, Appl. Surf. Sci. 373 (2019) 578–588.

[12] C.Z. Jin, Y.J. Wang, H.L. Tang, H.S. Wei, X. Liu, J.H. Wang, Synthesis, characterization, and catalytic applications of core-shell magnetic carbonaceous nanocomposites, J. Phys. Chem. C 118 (2014) 25110–25117.

[13] Q. Zhang, I. Lee, J.B. Joo, F. Zaera, Y.D. Yin, Core-shell nanostructured catalysts, Acc. Chem. Res. 46 (2013) 1816–1824.

[14] R.G. Chaudhuri, S. Paria, Core/shell nanoparticles: classes, properties, synthesis mechanisms, characterization, and applications, Chem. Rev. 112 (2012) 2373–2433.

[15] W.J. An, L.Y. Tian, J.S. Hu, L. Liu, W.Q. Cui, Y.H. Liang, Efficient degradation of organic pollutants by catalytic ozonation and photocatalysis synergy system using double-functional MgO/g-C_3N_4 catalyst, Appl. Surf. Sci. 534 (2020) 147518.

[16] L.L. Chen, L. Li, T.T. Wang, L.Y. Zhang, S.X. Xing, C.G. Wang, Z.M. Su, A novel strategy to fabricate multifunctional $Fe_3O_4@C@TiO_2$ yolk-shell structures as magnetically recyclable photocatalysts, Nanoscale 6 (2014) 6603–6608.

[17] Y.H. Deng, Y. Cai, Z.K. Sun, J. Liu, C. Liu, J. Wei, W. Li, C. Liu, Y. Wang, D.Y. Zhao, Multifunctional mesoporous composite microspheres with well-designed nanostructure: a highly integrated catalyst system, J. Am. Chem. Soc. 132 (2010) 8466–8473.

[18] Q. Yue, J.L. Li, Y. Zhang, X.W. Cheng, X. Chen, P.P. Pan, J.C. Su, A.A. Elzatahry, A. Alghamdi, Y.H. Deng, D.Y. Zhao, Plasmolysis-lnspired nanoengineering of functional yolk-shell microspheres with magnetic core and mesoporous silica Shell, J. Am. Chem. Soc. 139 (2017) 15486–15493.

[19] S. Khammar, N. Bahramifar, H. Younesi, Preparation and surface engineering of CM- beta-CD functionalized Fe_3O_4@TiO_2 nanoparticles for photocatalytic degradation of polychlorinated biphenyls (PCBs) from transformer oil, J. Hazard. Mater. 394 (2020) 122422.

[20] K.P. Yuan, R.C. Che, Q. Cao, Z.K. Sun, Q. Yue, Y.H. Deng, Designed fabrication and characterization of three-dimensionally ordered arrays of core-shell magnetic mesoporous carbon microspheres, ACS Appl. Mater. Interfaces 7 (2015) 5312–5319.

[21] J. Han, S. Lu, C.J. Jin, M.G. Wang, R. Guo, Fe_3O_4/PANI/m-SiO_2 as robust reactive catalyst supports for noble metal nanoparticles with improved stability and recyclability, J. Mater. Chem. A 2 (2014) 13016–13023.

[22] Y. Yang, W.J. Zhu, B.F. Shi, C.L. Lu, Construction of a thermo-responsive polymer brush decorated Fe_3O_4@catechol-formaldehyde resin core-shell nanosphere stabilized carbon dots/Pd NP nanohybrid and its application as an efficient catalyst, J. Mater. Chem. A 8 (2020) 4017–4029.

[23] T. Zeng, X.L. Zhang, H.Y. Niu, Y.R. Ma, W.H. Li, Y.Q. Cai, In situ growth of gold nanoparticles onto polydopamine-encapsulated magnetic microspheres for catalytic reduction of nitrobenzene, Appl. Catal. B-Environ. 134 (2013) 26–33.

[24] J. Zhou, H. Zhou, Y. Zhang, J. Wu, H. Zhang, G. Wang, J. Li, Pseudocapacitive deionization of uranium(VI) with WO_3/C electrode, Chem. Eng. J. 398 (2020).

[25] G.C. Xi, B. Yue, J.Y. Cao, J.H. Ye, Fe_3O_4/WO_3 hierarchical core-shell structure: high-performance and recyclable visible-light photocatalysis, Chem. – Eur. J. 17 (2011) 5145–5154.

[26] W. Al Zoubi, Y.G. Ko, Self-assembly of hierarchical N-heterocycles-inorganic materials into three-dimensional structure for superior corrosion protection, Chem. Eng. J. 356 (2019) 850–856.

[27] E.S. Muckley, T. Aytug, R. Mayes, A.R. Lupini, J.Y. Carrillo, M. Goswami, B. G. Sumpter, I.N. Ivanov, Hierarchical TiO_2:Cu_2O nanostructures for gas/vapor sensing and CO_2 sequestration, ACS Appl. Mater. Interfaces 11 (2019) 48466–48475.

[28] C. de Vet, L. Gartzia-Rivero, P. Schafer, G. Raffy, A. Del Guerzo, Photocontrolled hierarchical self-assembly of anisotropic micropatterns of nanofibers onto isotropic surfaces, Small 16 (2020) 1906723.

[29] Z.X. Yan, Z.H. Xu, J.G. Yu, M. Jaroniec, Effect of microstructure and surface hydroxyls on the catalytic activity of Au/AlOOH for formaldehyde removal at room temperature, J. Colloid Interf. Sci. 501 (2017) 164–174.

[30] C.Z. Wang, Y.S. Jia, Z.Q. Zhang, G.F. Zhao, Y. Liu, Y. Lu, Role of PdCx species in Pd@PdCx/AlOOH/Al-fiber catalyst for the CO oxidative coupling to dimethyl oxalate, Appl. Surf. Sci. 478 (2019) 840–845.

[31] M. Tian, X.L. Cui, C.X. Dong, Z.P. Dong, Palladium nanoparticles dispersed on the hollow aluminosilicate microsphere@hierarchical γ-AlOOH as an excellent catalyst for the hydrogenation of nitroarenes under ambient conditions, Appl. Surf. Sci. 390 (2016) 100–106.

[32] X.L. Yang, X.Y. Wang, Y.Q. Feng, G.Q. Zhang, T.S. Wang, W.G. Song, C.Y. Jiang, L. Shu, C.R. Wang, Removal of multifold heavy metal contaminations in drinking water by porous magnetic Fe_2O_3@AlO(OH) superstructure, J. Mater. Chem. A 1 (2013) 473–477.

[33] Z. Yan, L. Fu, H. Yang, J. Ouyang, Amino-functionalized hierarchical porous SiO_2-AlOOH composite nanosheets with enhanced adsorption performance, J. Hazard. Mater. 344 (2018) 1090–1100.

[34] Y.X. Zhang, Y. Jia, Z. Jin, X.Y. Yu, W.H. Xu, T. Luo, B.J. Zhu, J.H. Liu, X.J. Huang, Self-assembled, monodispersed, flower-like gamma-AlOOH hierarchical superstructures for efficient and fast removal of heavy metal ions from water, CrystEngComm. 14 (2012) 3005–3007.

[35] X.L. Cui, Y.F. Zheng, M. Tian, Z.P. Dong, Novel yolk–shell-structured Fe_3O_4@ γ-AlOOH nanocomposite modified with Pd nanoparticles as a recyclable catalyst with excellent catalytic activity, Appl. Surf. Sci. 416 (2017) 103–111.

[36] L.F. Bai, W.Q. Jiang, M. Liu, S. Wang, M. Sang, S.H. Xuan, X.L. Gong, General and facile method to fabricate yolk-like structural magnetic nanocatalysts, ACS Sustain. Chem. Eng. 6 (2018) 8274–8284.

[37] Y.W. Zhang, M. Zhang, J.B. Yang, L. Ding, J. Zheng, J.L. Xu, S.L. Xiong, Formation of Fe_3O_4@SiO_2@C/Ni hybrids with enhanced catalytic activity and histidine-rich protein separation, Nanoscale. 8 (2016) 15978–15988.

[38] K.Z. Xu, J. Wu, Q.L. Fang, L.F. Bai, J.Y. Duan, J.X. Li, H.J. Xu, A.L. Hui, L.Y. Hao, S. H. Xuan, Magnetically separable h-Fe3O4@Au/polydopamine nanosphere with a hollow interior: A versatile candidate for nanocatalysis and metal ion adsorption, Chem. Eng. J. 398 (2020).

[39] S.H. Xuan, F. Wang, X.L. Gong, S.K. Kong, J.C. Yu, K.C.F. Leung, Hierarchical core/shell Fe_3O_4@SiO_2@gamma-AlOOH@Au micro/nanoflowers for protein immobilization, Chem. Commun. 47 (2011) 2514–2516.